Dynamic electron density as an order parameter for phase transitions: Evidence from α-KNO_3

Anagha Ghosh [1], Somnath Dey [2,*], B. Viliam Hakala [3], Hend Shahed [3], Sander van Smaalen [4], and Swastik Mondal [1,5,†]

[1] *CSIR—Central Glass and Ceramic Research Institute, 196, Raja S. C. Mullick Road, Jadavpur, Kolkata 700032, India*

[2] *Institute of Crystallography, RWTH Aachen University, Aachen 52066, Germany*

[3] *Jülich Centre for Neutron Science, Forschungszentrum Jülich, Jülich 52425, Germany*

[4] *Laboratory of Crystallography, Bayerisches Geoinstitut, University of Bayreuth, Bayreuth 95440, Germany*

[5] *Academy of Scientific and Innovative Research (AcSIR), Ghaziabad 201002, India*

(Received 3 February 2026; accepted 13 October 2026; published 5 November 2026)

We report that topological features of the dynamic electron density provide a microscopic electronic order parameter that directly reflects the extent of structural change during a phase transition and offers insight into its underlying mechanism. Using multipole electron-density models derived from extensive high-resolution synchrotron x-ray diffraction datasets collected on α-KNO_3 at 100, 200, 290, and 380 K, we reconstruct the thermally convoluted dynamic electron density at each temperature. It is found that its temperature evolution quantitatively captures the progressive suppression of local symmetry breaking as the system approaches the $\alpha \rightarrow \beta$ phase transition. The topological descriptors of the electron density associated with the nitrate group exhibit a nonmonotonic temperature evolution with the initial inequivalence among the N–O bond electron densities undergoing an order-parameter-like collapse upon heating to 380 K, preceding the actual phase-transition temperature. These findings demonstrate that dynamic electron-density topology can provide valuable microscopic insight into structural phase transitions.

DOI: 10.1103/vjv9-twm9

I. INTRODUCTION

Structural phase transitions (SPTs) in solids are conventionally described within the Landau-Ginzburg-Wilson framework of spontaneous symmetry breaking, in which an order parameter (OP) characterizes the emergence of a low-symmetry phase from a high-symmetry state [1,2]. In crystalline materials, such transitions are typically classified using geometric order parameters, including spontaneous lattice strain, atomic displacement parameters, and molecular orientations, as extracted from diffraction experiments and spectroscopic probes [3–5]. While these quantities reliably identify broken-symmetry phases, they provide only indirect insight into the microscopic

[*] Present address: Department of Structure Analysis, Institute of Physics of the Czech Academy of Sciences, Prague 8 18221, Czech Republic.

[†] Contact author: swastik_mondal@cgcri.res.in

Published by the American Physical Society under the terms of the Creative Commons Attribution 4.0 International license. Further distribution of this work must maintain attribution to the author(s) and the published article's title, journal citation, and DOI.

mechanisms that drive the instability. At a fundamental level, structural transformations originate from rearrangements of electron density, which govern interatomic forces, bonding anisotropy, and lattice stability. The recognition of electronically driven phase transitions, such as Peierls instabilities in low-dimensional conductors [6], correlation-induced Mott transitions in transition-metal oxides [7] and charge-density-wave formation [8], has shifted attention toward electronic degrees of freedom as a primary driver of phase transitions in solids. Despite this recognition, most experimental studies of SPTs rely on structural OPs derived from average nuclear positions [9,10]. This limitation is most evident near phase boundaries, where finite-temperature anharmonic fluctuations invalidate harmonic approximations and obscure electronic signatures of the emerging phase. In order-disorder systems, diffraction probes thermally averaged structures that may retain an apparently high lattice symmetry even when local environments fluctuate strongly, rendering conventional structural order parameters insensitive to transient bonding anisotropy and local polarization [11–13]. Because electron density directly encodes interatomic bonding and energetics [14–16], its temperature-dependent evolution provides a natural microscopic probe of structural instability. Thermal motion dynamically modulates the spatial distribution of the electron density, such that models derived from low-temperature static structures may be inaccurate with respect to a finite-temperature bonding anisotropy that precedes a phase transition [17–19]. Experimentally, the thermally averaged electron density is reconstructed from structure factors in which thermal motion is incorporated through anisotropic displacement parameters, followed by inverse Fourier transformation [20].

In this work, we employ dynamic electron density to investigate the microscopic origin of the temperature-induced structural phase transition in α-KNO_3, a prototypical periodic crystal undergoing a well-characterized $\alpha \rightarrow \beta$ transformation at 401 K. This transition involves a symmetry change from *Pnma* to $R\bar{3}m$ and is dominated by rotational disorder of the NO_3^- groups within the crystal-field potential generated by surrounding K^+ ions [21]. Previous diffraction, spectroscopic, and simulation studies have established the presence of strong lattice anharmonicity and nitrate reorientation across the transition [21–27]. By explicitly incorporating thermal motion into multipole model-based diffraction-derived electron densities, we reveal a temperature-dependent redistribution of electron density that precedes the macroscopic symmetry change. Our results identify the electronic precursors governing the $\alpha \rightarrow \beta$ transition and establish dynamic electron density as a powerful experimental framework for probing phase-transition mechanisms in crystalline materials.

II. METHODS

A. Experimental details

High-quality single crystals were obtained from aqueous solution through slow evaporation and subsequent repetitive recrystallization. Single-crystal x-ray diffraction data were collected from the same crystal ($0.19 \times 0.21 \times 0.24\,mm^3$) at four temperatures (100, 200, 290, and 380 K) maintaining unique orientation to enable accurate comparison of the temperature-dependent evolution of electron density in dynamic electron-density analysis. The x-ray beam size at the sample position was $0.4 \times 0.4\,mm^2$. Diffraction data at all temperatures were collected using a combination of ϕ- and ω-scan strategies with a rotation step of 0.5° per frame. Exposure times of 0.25 and 1.0 s per frame were used, depending on the scan mode and the diffraction intensity requirements. Measurements above 380 K were not performed for high-resolution electron-density analysis due to the upper temperature stability limit of the synchrotron experimental setup. Measurements were performed on a Huber four-circle κ diffractometer equipped with a Pilatus 1M detector at beamline P24, PETRA III (DESY, Hamburg), using synchrotron radiation ($\lambda = 0.5000$ Å). The crystal temperature was controlled using an Oxford Cryostream 700 cryostat. Cooling and heating rates were maintained @ $240\,K\,h^{-1}$ and @ $100\,K\,h^{-1}$ 10 K prior to and till target temperatures with equilibration times of 2 and 5 min, respectively. Complete datasets were collected up to $\sin\theta/\lambda = 1.15\,Å^{-1}$. Data processing were performed using CrysAlis^{Pro} [28], resulting in 2221 unique reflections ($R_{int} = 0.0397$) at

100 K after outlier rejection. Initial structure solution was carried out with the WinGX package [29] via direct methods by SHELXS [30] and the model was subsequently refined by SHELXL [30] yielding good fit to the diffraction data [$R(F) = 0.0225$, $wR_{F^2} = 0.0639$, and $S = 1.100$ at 100 K]. Equivalent refinement protocols were applied at higher temperatures ensuring consistency of high-resolution electron-density reconstructions. Independent spherical atom refinement of the β phase of KNO_3 using single-crystal in-house x-ray diffraction data collected at 400 ± 2 K exhibits strong disorder of the nitrate groups; details are provided in the Supplemental Material [31]. Such disorder prevents reliable electron-density refinement using multipole model and hence was not considered further in this study.

Aspherical atom refinements on F^2 were performed against the 100 K data, using the XD2024 [33] software package employing the Hansen-Coppens multipole formalism with scattering factors from the SCM databank [34]. High-order ($0.80\,\text{Å}^{-1} < \sin\theta/\lambda < 1.08\,\text{Å}^{-1}$) 271 reflections were used to accurately determine atomic coordinates and anisotropic displacement parameters. Refinement proceeded through sequential optimization of the scale factor, monopole populations, and higher multipole terms up to hexadecapoles, followed by iterative refinement of positional and anisotropic displacement parameters. κ parameters were refined for nitrogen ($\kappa = 0.995$) and oxygen ($\kappa = 0.994$), while that for potassium was fixed to 1. An isotropic type-I extinction correction was applied throughout. The final multipole model (Appendix) converged with excellent residual values $R(F) = 0.0165$, $wR(F) = 0.0197$ [$w = 1/\sigma^2(F^2)$] and $S = 1.06$. Residual density map was largely featureless with densities $+0.25$ and $-0.26\,\text{e Å}^{-3}$ confined to the O1–N1–O2 molecular plane [Fig. 2(b)]. Topological analysis was performed using XDPROP [33], yielding charge imbalance of an approximately 0.003 e, while the sum of atomic basin volumes reproduced the unit-cell volume (V_{cell}) within a relative error of less than 0.33% (Table S3 in the Supplemental Material [31]).

B. Computational details

The time-average electron density of a crystal with N_{atom} atoms in the unit cell is defined as

$$\langle \rho(\mathbf{r}) \rangle = \sum_{\mathbf{L}}^{\text{Volume}} \sum_{\mu=1}^{N_{\text{atom}}} \int \rho_\mu\left(\mathbf{r} - \mathbf{L} - \mathbf{r}_\mu^0 - \mathbf{u}_\mu\right) P(\mathbf{u}_\mu) d\mathbf{u}_\mu, \tag{1}$$

where $\rho_\mu(\mathbf{r} - \mathbf{L} - \mathbf{r}_\mu^0 - \mathbf{u}_\mu)$ is the static electron density of atom μ displaced by $\mathbf{u}_\mu$ from its equilibrium position $\mathbf{r}_\mu^0$ in unit cell L and $P(\mathbf{u}_\mu)$ is the displacement probability density. Within the harmonic approximation, the corresponding structure factor is

$$F(\mathbf{H}) = \sum_{\mu=1}^{N_{\text{atom}}} f_\mu(\mathbf{H}) \exp(-2\pi^2 \mathbf{H}^{\mathrm{T}} \mathbf{U}_\mu \mathbf{H}) \exp\left(2\pi i \mathbf{H} \cdot \mathbf{r}_\mu^0\right), \tag{2}$$

where $f_\mu(\mathbf{H})$ denotes the aspherical atomic scattering factor, $\mathbf{U}_\mu$ is the anisotropic displacement parameter (ADP) tensor, and

$$\mathbf{H} = h\mathbf{a}^* + k\mathbf{b}^* + l\mathbf{c}^*. \tag{3}$$

The dynamic electron density is obtained via inverse Fourier transform,

$$\rho_T(\mathbf{r}) = \left(\frac{1}{V_{\text{cell}}}\right) \sum_{j=1}^{N_{\text{ref}}} F(\mathbf{H}_j) \exp(-2\pi i\, \mathbf{H}_j \cdot \mathbf{r}). \tag{4}$$

Structure factors are evaluated on a uniform fast Fourier transform grid with $N_{\text{pix}} = N_1 \times N_2 \times N_3$ and $h_{\max} \cong \frac{N_1}{2}$ (similarly for k and l). The relationship between maximum resolution of the

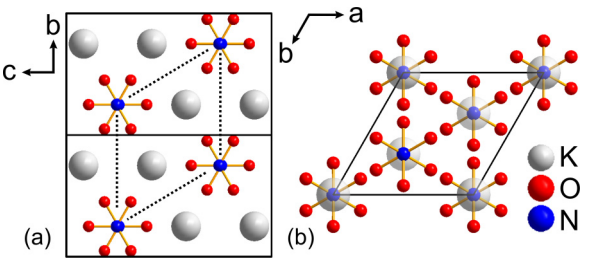


FIG. 1. (a) Crystal structure of α-KNO_3; the pseudohexagonal unit cell is related to that of β-KNO_3. (b) Crystal structure of β-KNO_3, showing dynamic disorder between two NO_3^- orientations at each site.

reflections and grid size is [20]

$$\left[\frac{\sin\theta}{\lambda}\right]_{\max} \cong \frac{0.25}{\text{grid size}}. \tag{5}$$

While experimental data typically extend to 1.3 $Å^{-1}$, model structure factors were computed up to $[\frac{\sin\theta}{\lambda}]_{\max} \cong 12.5\,Å^{-1}$ using grid spacing of 0.02 Å using computer program PRIOR [20]. A full multipole refinement was performed at 100 K. At 200, 290, and 380 K, the multipole parameters were constrained to their 100 K values, following an approach analogous to the invariom strategy [20,35–38]. Dynamic deformation densities were computed as differences between dynamic multipole and independent atom model densities. Density maps were generated with JANA2006 [39], and topological properties and atomic charges (Table II) were derived from these dynamic densities using EDMA [40].

III. RESULTS AND DISCUSSION

At room temperature, α-KNO_3 adopts an orthorhombic *Pnma* (No. 62) structure. Upon heating, the α phase transforms at 401 K into the β phase, which has a trigonal $R\bar{3}m$ (No. 166) structure and a larger volume per molecule [Figs. 1(a) and 1(b)]. The β phase is orientationally disordered, with nitrate ions dynamically fluctuating between two orientations related by 60° rotations about the trigonal axis; the oxygen atoms exhibit 50% occupancy, reflecting dynamic disorder arising from correlated NO_3^- rotations. The $\alpha \rightarrow \beta$ transition also involves coordinated K^+ displacements and pronounced anisotropic expansion along the *a* axis [21,22]. To elucidate the microscopic electronic signatures associated with this transformation, temperature-dependent dynamic electron densities have been reconstructed from high-quality synchrotron datasets collected at 100, 200, 290, and 380 K. This approach enables direct monitoring of temperature-induced topological variations in the electron density within the α phase.

At 100 K, static and dynamic electron densities exhibit very good agreement in atomic maxima positions for K, N, and O (Table S2 in the Supplemental Material [31]), although dynamic electron density shows diminished peak heights arising from thermal motion and zero-point vibrational smearing [20]. The deformation density maps at 100 K similarly reveal pronounced N–O and K–O bonding resembling the static counterparts, with progressive flattening and thermal smearing observed at elevated temperatures [Figs. 2(e)–2(h)]. Bond critical points (BCPs) are consistently identified for all covalent and ionic bonds at 100 K, with positions matching closely with their static counterparts [Figs. 2(d) and 2(e)], confirming the reliability of our dynamic electron-density calculations. The temperature dependence of the electron density values at these BCPs is also notable. Quantitatively, for the N–O bonds at 100 K, ρ_T(BCP) is smaller in dynamic density than in the static density by roughly 0.29 e $Å^{-3}$, while K–O bonds show a slight decrease of about 0.02–0.03 e $Å^{-3}$, reflecting redistribution of electron density from high-density to low-density regions induced by thermal vibrations (Table I). From static density at 100 K and the dynamic density

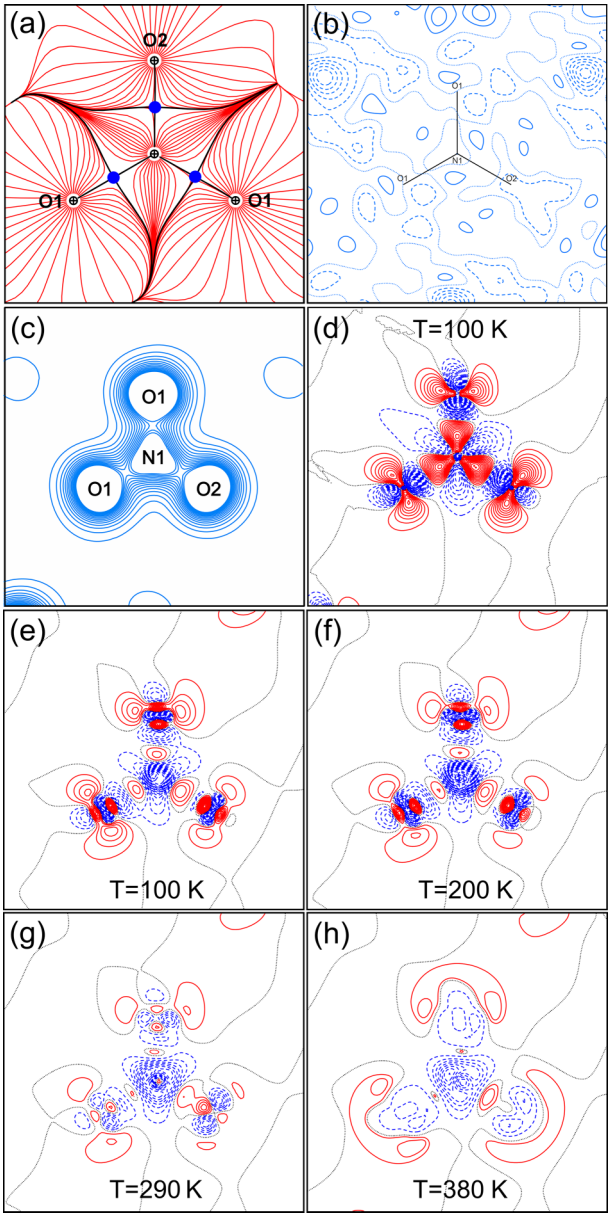


FIG. 2. Multipole electron density of α-KNO_3 at 100 K. (a) Gradient trajectories of the N basin in the static density; (3, −1) critical points are marked in blue. Section: 6×6 Å^2 centered on O1–O2–O1. (b) Residual density ($\sin\theta/\lambda \leqslant 1.06$ Å^{-1}; 0.05 e Å^{-3}). (c) Static density (contours from 0.25 to 3.5 e Å^{-3}). (d) Static deformation density (0.05 e Å^{-3}). (e)–(h) Dynamic deformation density in the O1–O2–O1 plane at four temperatures (contour interval 0.05 e Å^{-3}); solid red, dashed blue, and dotted black lines indicate positive, negative, and zero contours, respectively.

at 290 K, the ρ_T(BCP) values for both N1–O1 and N1–O2 bonds decrease monotonically, showing reductions of approximately 0.56 and 0.50 e Å^{-3}, respectively. Consistent with this interpretation, the refined anisotropic displacement parameters U_{ij} increase monotonically with temperature for all atoms, with $U_{ij}[T = 380\ \text{K}] > U_{ij}[T = 290\ \text{K}]$ in every case (Table S4 in the Supplemental

TABLE I. Comparison of electron densities and Laplacians at N–O and K–O bond critical points between the static multipole density (100 K) and dynamic multipole densities of α-KNO_3 at four different temperatures.

	100 K (static)	100 K (dyn)	200 K (dyn)	290 K (dyn)	380 K (dyn)
			N1–O1/N1–O2		
ρ	3.078(2)/3.141(8)	2.7592/2.8858	2.6104/2.7965	2.5130/2.6376	2.8800/2.9074
$\nabla^2\rho$	−4.606(87)/−7.131(72)	−2.0177/−4.9473	−2.0667/−4.3888	4.5048/6.6644	18.3860/21.5641
			K1–O1/K1–O2		
ρ	0.124(1)/0.106(1)	0.1020/0.0799	0.1044/0.0820	0.1144/0.0869	0.1203/0.1002
$\nabla^2\rho$	0.092(13)/1.138(10)	1.4879/1.4013	1.5279/1.4341	1.7064/1.5371	1.7739/1.7519

Material [31]). This continuous thermal smearing is disrupted by a pronounced discontinuity at 380 K, where ρ_T(BCP) for both N–O bonds significantly increase to 0.37 e Å^{-3} for N1–O1 and 0.27 e Å^{-3} for N1–O2 relative to room temperature. Accompanying this increase, $\nabla^2\rho_T$(BCP) also rises sharply by roughly 13.9 and 14.9 e Å^{-5} for N1–O1 and N1–O2, respectively (Table I). The thermal evolution (100–290 K) can be understood through temperature-induced redistribution of electron density coupled with enhanced atomic vibrations. Thermal smearing causes electron density to increase along the bond path as atomic maxima broaden, while simultaneously depleting electron density in regions perpendicular to the bond. This explains that monotonic decrease in ρ_T(BCP) arises from increasing thermal effects. However, the nonmonotonic behavior of the electron density at 380 K cannot be attributed solely to the effects of thermal smearing. At 380 K, increasing orientational fluctuations and librational motion lead to a progressive averaging of the local N–O environments, resulting in an effective D3h-like electronic distribution as the phase transition is approached. This structural relaxation is governed by symmetry-driven redistribution of electron density along the N–O bond paths, leading to an increase in ρ_T(BCP).

On the other hand, the K–O bonds remain essentially unaffected across this interval, consistent with their dominantly electrostatic and ionic characters that are insensitive to local vibrational distortions (Fig. S3 in the Supplemental Material [31]). Considering topological curvature, the Laplacian $\nabla^2\rho_T$(BCP) for the N–O bonds remains negative at 100 and 200 K, indicative of concentrated, shared-shell covalent interactions. However, at 290 K, the Laplacian becomes positive (Table I). This sign reversal signifies that the BCP enters a rapidly varying region of the Laplacian surface, where small positional shifts of the BCP drastically influence Laplacian magnitude and sign [41]. Crucially, BCP locations shift by approximately 0.070 and 0.068 Å relative to static counterparts at 380 K. Throughout all these temperatures, oxygen atomic maxima remain consistently lower and more spatially diffuse than nitrogen maxima, consistent with oxygen's larger librational amplitude due to nitrate rotations with N atom staying fixed at the center [Figs. 3(a) and 3(b)]. Notably, this electronic resurgence coincides with an ∼4% lattice expansion along *a* axis from 100 to 380 K (Appendix), which reduces steric constraints between NO_3^- and K^+ layer, thereby

TABLE II. Charges from the basin integration for all atoms in α-KNO_3 at four different temperatures (dynamic).

Atom	100 K	200 K	290 K	380 K
K1	+0.772 02	+0.773 66	+0.774 88	+0.769 03
O1	−0.467 91	−0.466 60	−0.484 51	−0.442 52
O2	−0.470 50	−0.463 82	−0.495 20	−0.462 96
N1	+0.637 16	+0.651 06	+0.701 17	+0.601 54

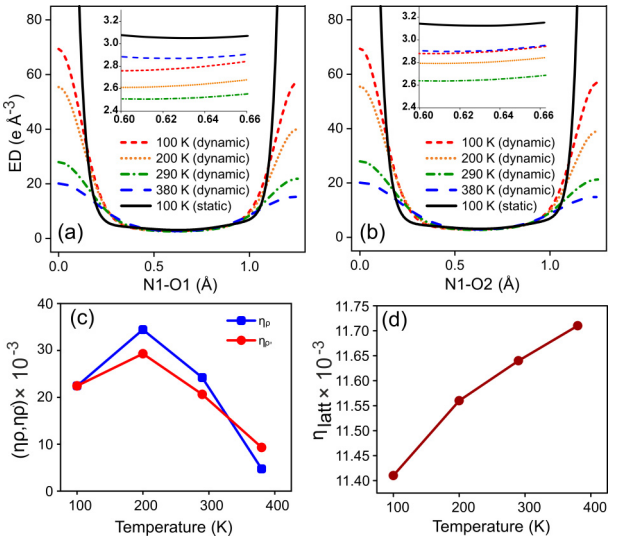


FIG. 3. (a), (b) Static and dynamic MP electron density profiles vs distance from the nuclei along the N1–O2 bond and N1–O1 bond, respectively. (c) Temperature dependence of the electronic order parameter, η_p, obtained from transferred (η_ρ, blue) and independently refined ($\eta_{\rho'}$, red) multipole models. (d) Temperature dependence of the spontaneous lattice strain, η_{latt}.

facilitating further enhanced nitrate rotational freedom. This interplay between lattice softening and electronic reorganization promotes further expansion of lattice parameters as the system approaches the critical transition temperature [21,22].

To quantify the electronic asymmetry between the two N–O bonds, we define a dimensionless electronic order parameter (η_ρ) based on the difference between the electron densities at the BCPs of a bond relevant to the phase transition. In case of KNO_3, η_ρ can be defined as

$$\eta_\rho = \frac{\rho_{\mathrm{BCP(N1-O2)}} - \rho_{\mathrm{BCP(N1-O1)}}}{\rho_{\mathrm{BCP(N1-O2)}} + \rho_{\mathrm{BCP(N1-O1)}}}, \tag{6}$$

where ρ_{BCP}(N1–O1) and ρ_{BCP}(N1–O2) are the dynamic electron densities at the bond critical points of the N1–O1 and N1–O2 bonds, respectively. The numerator represents the difference in the dynamic electron densities of the two bonds, while the denominator normalizes this difference, yielding a dimensionless order parameter. An η_ρ value of zero indicates electronically equivalent N–O bonds, whereas increasing $|\eta_\rho|$ reflects increasing electronic asymmetry. N1−O1 and N1−O2 bonds are equivalent by symmetry within the high-temperature phase. Therefore, ρ_{BCP}(N1–O1) = ρ_{BCP}(N1–O2) and $\eta_\rho = 0$ within the high-temperature phase.

The magnitude of η_ρ remains finite in the low-temperature regime, with values of 0.022 at 100 K and a maximum of 0.034 at 200 K, followed by a reduction to 0.024 at 290 K. At 380 K, η_ρ collapses to a near-zero value of 0.005, indicating the near-equivalent N–O bond character close to the phase transition. The estimated standard uncertainties of η_p were evaluated based on the 100 K static multipole model, since the low-temperature multipole parameters were used to generate the higher-temperature dynamic electron densities, while additional uncertainties arising from the temperature-dependent ADPs were found to be considerably smaller than those associated with the static multipole model and therefore do not affect the qualitative conclusions. Under this approximation, all η_ρ values satisfy $\eta_\rho/\sigma(\eta_\rho) > 3$. To assess the robustness of this behavior against modeling assumptions, independent unconstrained multipole refinements were additionally performed at all temperatures. The resulting $\eta_{\rho'}$ values (Table S7 in the Supplemental Material [31]) reproduce the same qualitative temperature evolution obtained from the transferred multipole

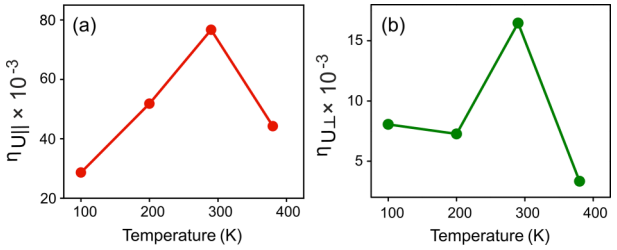


FIG. 4. Temperature dependence of the ADP-based vibrational descriptors: (a) $\eta_{U||}$ (bond-parallel asymmetry) and (b) $\eta_{U\perp}$ (bond-perpendicular asymmetry).

model, an increase between 100 and 200 K followed by a collapse near the phase-transition temperature [Fig. 3(c)]. The maximum difference between the two approaches remains below ∼0.005, indicating that the nonmonotonic behavior of η_ρ is not an artifact of the transferred multipole parameters. Within the high-temperature phase β-KNO_3, all oxygen atoms are equivalent by symmetry, and the order parameter has value zero. The small absolute magnitude of η_ρ is expected for chemically bonded N–O pairs; however, its pronounced temperature dependence demonstrates its high sensitivity to subtle electronic symmetry breaking within the nitrate group. To probe lattice coupling, we measure the spontaneous strain associated with deviations from the hexagonal matrix [42],

$$\eta_{\text{latt}} = \frac{b - c/\sqrt{3}}{b + c/\sqrt{3}}. \tag{7}$$

In contrast to η_ρ, η_{latt} varies only weakly, increasing monotonically from 0.011 41 at 100 K to 0.011 71 at 380 K [Figs. 3(c) and 3(d)]. To provide a local structural baseline for η_ρ, we also evaluated the bond-projected vibrational asymmetry parameter

$$\eta_{U||} = \frac{U_{||}(O_2) - U_{||}(O_1)}{U_{||}(O_2) + U_{||}(O_1)} \tag{8}$$

together with the transverse vibrational asymmetry parameter

$$\eta_{U\perp} = \frac{U_{\perp}(\mathrm{O}_2) - U_{\perp}(\mathrm{O}_1)}{U_{\perp}(\mathrm{O}_2) + U_{\perp}(\mathrm{O}_1)}, \tag{9}$$

derived from the anisotropic displacement tensors of the two crystallographically distinct oxygen atoms.

Between 100 and 200 K, the temperature evolution of η_ρ closely follows $\eta_{U||}$, whereas $\eta_{U\perp}$ remains nearly constant (Table S8 in the Supplemental Material [31]). This behavior indicates that the dominant structural evolution in this temperature range arises from the increasing difference in the bond-parallel mean-square displacements of the two oxygen atoms, suggesting that η_ρ primarily reflects the local bond-parallel asymmetry within the nitrate group in the low-temperature regime [Figs. 4(a) and 4(b)]. Between 200 and 290 K, the magnitude of $\eta_{U\perp}$ increases much more rapidly, from 0.0072 to 0.0165 (≈2.3-fold), because the perpendicular mean-square displacement of O1 increases substantially relative to that of O2. Since the dynamic electron density is obtained by convolution of the static electron density with the three-dimensional atomic displacement probability distribution defined by the ADPs, the increasingly dominant perpendicular displacement of O1 becomes the additional factor governing the evolution of the bond critical point properties in this temperature range. The enhanced transverse vibrational anisotropy modifies the spatial distribution and curvature of the dynamic electron density around nitrate group, leading to changes in the Laplacian at bond critical points while simultaneously reducing the difference between the electron densities of the two N–O bond critical points, thereby causing the decrease of η_ρ, where the fixed-BCP linearization holds. Above 290 K, however, this approximation is no longer

valid because both N–O bond critical points are displaced by approximately 0.07 Å at 380 K. The BCP migrations, which themselves arise from enhanced thermal fluctuations (Table S4 in the Supplemental Material [31]), result in nearly equivalent bond critical point environments, causing η_ρ to approach zero and reflecting the progressive loss of local electronic asymmetry as the high-symmetry β phase is approached. The phase transitions in KNO_3 are reversible and proceed through the sequence $R\bar{3}m$ (high-temperature β phase) $\rightarrow$ $R3m$ (intermediate-high ferroelectric γ phase) $\rightarrow$ *Pnma* (low-temperature α phase) [22]. The $\alpha \leftrightarrow \beta$ transition therefore represents a first-order reconstructive transformation between the orthorhombic *Pnma* and trigonal $R\bar{3}m$ structures, which are not related by a direct translationengleiche or klassengleiche group-subgroup relationship [43]. Consequently, the conventional Landau formalism based on a single symmetry-adapted order parameter belonging to an active irreducible representation of the parent phase is not directly applicable to this transition [44–46]. Nevertheless, the coupling between the orientational order parameter Q_S and the electronic order parameter η_ρ can be described phenomenologically through a free-energy expansion. Minimization of the free energy with respect to η_ρ yields $\eta_\rho = \frac{\lambda_1 {Q_S}^2}{a_\rho}$ showing that the electronic order parameter is induced by the orientational ordering of the nitrate groups, with the detailed calculations provided in the Supplemental Material [31]. In this context, η_ρ should be regarded as an electronic quantity coupled to the underlying orientational and structural evolution of the nitrate groups. Therefore, η_ρ satisfies the essential symmetry requirement of vanishing in the high-symmetry β phase, where all oxygen atoms become crystallographically equivalent.

Thus, the temperature-dependent topological evolution of dynamic electron density around the N–O bonds serves as a sensitive probe of the thermally induced order-disorder transition in α-KNO_3, directly connecting microscopic electron redistribution to macroscopic crystallographic changes. These findings establish topological properties of dynamic electron density derived from the multipole model as a quantitative descriptor of the underlying structural phase transitions.

IV. CONCLUSION

In conclusion, this work provides the first experimental evidence that the dynamic electron density derived from multipole model can reveal the electronic precursors of a structural phase transition. In α-KNO_3, temperature-dependent analyses show a progressive destabilization of the nitrate N–O bonds well below the $\alpha \rightarrow \beta$ transition, highlighting dynamic electron density as a powerful probe of phase-transition physics. A pronounced weakening of the covalent N–O interactions is observed, followed at 380 K by clear topological signatures of incipient orientational disorder that immediately precede the structural transformation at 401 K. This behavior is consistent with the emergence of a precursor fluctuation regime, in which increasing thermal lattice vibrations and unit-cell expansion promote dynamic fluctuations of the nitrate groups, causing the symmetry-distinct local electronic environments to become nearly indistinguishable. This interpretation is further supported by Raman studies showing that the asymmetry of the 52 cm^{-1} Raman-active lattice translational mode increases continuously with temperature, reaches a maximum near 390 K, and disappears abruptly at the $\alpha \rightarrow \beta$ transition ($\sim$401 K), reflecting enhanced dynamic disorder associated with fluctuating nitrate-group orientations [47]. These results demonstrate that the dynamic density is not simply a vibrationally broadened static model but a physically meaningful finite-temperature electron-density distribution that directly captures the coupling between atomic motion and electronic rearrangement. The temperature evolution of bond critical points and Laplacian values provides a quantitative measure of emerging electronic instability, indicating that continuous changes in electronic topology accompany the approach to the structural transition. Accordingly, the topological properties of dynamic electron density can be regarded as an intrinsic electronic order parameter associated with structural phase transitions, offering a new framework for linking lattice dynamics, bond evolution, and electronic instabilities in temperature-driven structural transformations.

ACKNOWLEDGMENTS

The authors acknowledge financial support from the Department of Science and Technology, Government of India (DST), under the framework of the India@DESY collaboration. Beam time was allocated at P24, PETRA III, DESY for proposal I-20191344. The authors thank Carsten Paulmann for his assistance for the experiment at beamline P24. The authors also thank Prof. Anatoliy Volkov for helpful discussions related to the XD2024 software and Pratap Das for technical assistance. A.G. would like to acknowledge DST, Government of India for the INSPIRE fellowship (IF200309). S.M. would like to acknowledge financial support from SERB Core Research Grant, Government of India (Grant No. CRG/2023/002697). S.D. acknowledges postdoctoral research fellowship from Alexander von Humboldt foundation.

DATA AVAILABILITY

CIFs are included in the Supplemental Material [31]. Other data that support the findings of this article are not publicly available. The data are available from the authors upon reasonable request.

APPENDIX

Crystallographic data and refinement details for α-KNO_3 at different temperatures.

Crystal data	100 K	200 K	290 K	380 K
Compound formula	α-KNO_3	α-KNO_3	α-KNO_3	α-KNO_3
a (Å)	6.2751(1)	6.3583(1)	6.4636(3)	6.5247(3)
b (Å)	5.3925(1)	5.4038(1)	5.4226(1)	5.4121(3)
c (Å)	9.1293(2)	9.1457(2)	9.1760(1)	9.1570(5)
V (Å^3)	308.92(10)	314.24(10)	321.61(16)	323.35(3)
Z	4	4	4	4
λ (Å)	0.5	0.5	0.5	0.5
$[\sin(\theta)/\lambda]_{\text{full}}$ (Å^{-1})	1.10	1.10	1.00	1.00
Number of unique data	2221	2080	1438	1445
R_{int}	0.0397	0.0552	0.0409	0.0250
	Independent atom model			
Number of data in refinement	2221	2080	1438	1445
R_F (obs/all)	0.0214/0.0225	0.0234/0.0300	0.0247/0.0362	0.0294/0.0430
wR_{F^2} (all data)	0.0554	0.0623	0.0746	0.0985
$\Delta\rho_{\min}/\Delta\rho_{\max}$ (e Å^{-3})	−0.46/0.45	−0.64/0.54	−0.32/0.43	−0.30/0.51
Goodness of fit on F^2, S	1.047	1.000	1.089	1.070
	Multipole refinement			
R_F (obs/all)	0.0165/0.0180	0.0187/0.0279	0.0209/0.0298	0.0246/0.0388
wR_{F^2} (obs/all)	0.0197 (0.0396)	0.0246 (0.0491)	0.0263 (0.0540)	0.0392 (0.0675)
$\Delta\rho_{\min}/\Delta\rho_{\max}$ (e Å^{-3})	−0.258/0.254	−0.260/0.290	−0.324/0.330	−0.325/0.298
Goodness of fit on F^2, S	1.0610	1.1603	1.2028	1.4421

S denotes the conventional goodness-of-fit parameter defined as $S = [\frac{\sum w(F_o^2 - F_c^2)^2}{(n-p)}]^{1/2}$, where F_o and F_c are the observed and calculated structure-factor amplitudes, respectively, w is the weight assigned to each reflection, n is number of reflections, and p is the number of refined parameters.

[1] B. Horovitz, R. J. Gooding, and J. A. Krumhansl, Order parameters for reconstructive phase transitions, Phys. Rev. Lett. **62**, 843 (1989).
[2] J. C. Thomas and A. Van der Ven, Order parameters for symmetry-breaking structural transitions: The tetragonal-monoclinic transition in ZrO_2, Phys. Rev. B **96**, 134121 (2017).
[3] M. A. Carpenter, R. E. A. McKnight, C. J. Howard, and K. S. Knight, Symmetry and strain analysis of structural phase transitions in $Pr_{0.48}Ca_{0.52}MnO_3$, Phys. Rev. B **82**, 094101 (2010).
[4] J. Duboisset and P.-F. Brevet, Salt-induced long-to-short range orientational transition in water, Phys. Rev. Lett. **120**, 263001 (2018).
[5] T. Weigel, C. Richter, M. Nentwich, E. Mehner, V. Garbe, L. Bouchenoire, D. Novikov, D. C. Meyer, and M. Zschornak, Picometer atomic displacements behind ferroelectricity in the commensurate low-temperature phase in multiferroic YMn_2O_5, Phys. Rev. B **109**, 054101 (2024).
[6] R. H. McKenzie, Microscopic theory of the pseudogap and Peierls transition in quasi-one-dimensional materials, Phys. Rev. B **52**, 16428 (1995).
[7] H. Watanabe, T. Shirakawa, and S. Yunoki, Microscopic study of a spin-orbit-induced Mott insulator in Ir oxides, Phys. Rev. Lett. **105**, 216410 (2010).
[8] Y. Chen, C. Liang, J. Yuan, B. Wang, and H. Li, Unveiling the microscopic dynamics of the charge density wave transition in monolayer VX_2 (X = S, Te), Phys. Rev. B **109**, L140105 (2024).
[9] A. Benassi, A. Vanossi, G. E. Santoro, and E. Tosatti, Sliding over a phase transition, Phys. Rev. Lett. **106**, 256102 (2011).
[10] J. Kong, J. Liu, F. Marlton, M. R. V. Jørgensen, and A. Pramanick, Local structural mechanism for phase transition and ferroelectric polarization in the mixed oxide $K_{0.5}Na_{0.5}NbO_3$, Phys. Rev. B **103**, 184104 (2021).
[11] A. Bencan, E. Oveisi, S. Hashemizadeh, V. K. Veerapandiyan, T. Hoshina, T. Rojac, M. Deluca, G. Drazic, and D. Damjanovic, Atomic scale symmetry and polar nanoclusters in the paraelectric phase of ferroelectric materials, Nat. Commun. **12**, 3509 (2021).
[12] M. Baake and U. Grimm, Kinematic diffraction is insufficient to distinguish order from disorder, Phys. Rev. B **79**, 020203 (2009).
[13] H. Tong, P. Tan, and N. Xu, From crystals to disordered crystals: A hidden order-disorder transition, Sci. Rep. **5**, 15378 (2015).
[14] S. Mondal, S. van Smaalen, G. Parakhonskiy, S. J. Prathapa, L. Noohinejad, E. Bykova, N. Dubrovinskaia, D. Chernyshov, and L. Dubrovinsky, Experimental evidence of orbital order in α-B_{12} and γ-B_{28} polymorphs of elemental boron, Phys. Rev. B **88**, 024118 (2013).
[15] S. Mondal, S. van Smaalen, A. Schönleber, Y. Filinchuk, D. Chernyshov, S. I. Simak, A. S. Mikhaylushkin, I. A. Abrikosov, E. Zarechnaya, L. Dubrovinsky, and N. Dubrovinskaia, Electron-deficient and polycenter bonds in the high-pressure γ-B_{28} phase of boron, Phys. Rev. Lett. **106**, 215502 (2011).
[16] I. Inoue, Y. Deguchi, B. Ziaja, T. Osaka, M. M. Abdullah, Z. Jurek, N. Medvedev, V. Tkachenko, Y. Inubushi, H. Kasai, K. Tamasaku, T. Hara, E. Nishibori, and M. Yabashi, Atomic-scale visualization of ultrafast bond breaking in X-ray-excited diamond, Phys. Rev. Lett. **126**, 117403 (2021).
[17] Y. Ivanov, T. Nimura, and K. Tanaka, Electron density and electrostatic potential of $KMnF_3$: A phase-transition study, Acta Crystallogr. Sect. B **60**, 359 (2004).
[18] A. Poulain, E. Wenger, P. Durand, K. N. Jarzembska, R. Kamiński, P. Fertey, M. Kubicki, and C. Lecomte, Anharmonicity and isomorphic phase transition: A multi-temperature x-ray single-crystal and powder diffraction study of 1-(2′-aminophenyl)-2-methyl-4-nitroimidazole, IUCrJ **1**, 110 (2014).
[19] G. W. Howieson, K. K. Mishra, A. S. Gibbs, R. S. Katiyar, J. F. Scott, F. D. Morrison, and M. Carpenter, Structural phase transitions in the geometric ferroelectric $LaTaO_4$, Phys. Rev. B **103**, 014119 (2021).
[20] S. Mondal, S. J. Prathapa, and S. van Smaalen, Experimental dynamic electron densities of multipole models at different temperatures, Acta Crystallogr. Sect. A **68**, 568 (2012).
[21] J. Nimmo and B. Lucas, Conformation and orientation of NO_3 in α-phase potassium nitrate, Nat. Phys. Sci. **237**, 61 (1972).
[22] J. K. Nimmo and B. W. Lucas, The crystal structures of γ- and β-KNO_3 and the $\alpha \leftarrow \gamma \leftarrow \beta$ phase transformations, Acta Crystallogr. Sect. B **32**, 1968 (1976).

[23] H. M. Lu and J. R. Hardy, First-principles study of phase transitions in KNO_3, Phys. Rev. B **44**, 7215 (1991).
[24] W. Smith and J. H. R. Clarke, A molecular dynamics study of the crystalline phases of potassium nitrate, J. Chem. Phys. **90**, 6610 (1989).
[25] F. Brehat and B. Wyncke, Analysis of the temperature-dependent lattice modes in potassium nitrate by infrared spectroscopy, J. Phys. C Solid State Phys. **21**, 689 (1988).
[26] M. J. Westphal, J. W. Wood, R. D. Redin, and T. Ashworth, Calorimetric and photoacoustic investigation of KNO_3 phase transitions, J. Appl. Phys. **73**, 7302 (1993).
[27] B. V. Schønwandt and H. J. Jakobsen, Phase transitions in KNO_3 studied by variable-temperature ^{15}N magic-angle spinning NMR spectroscopy, J. Solid State Chem. **145**, 10 (1999).
[28] CrysAlis^{Pro} (Agilent Technologies Ltd, Yarnton, 2014).
[29] L. J. Farrugia, WinGX suite for small-molecule single-crystal crystallography, J. Appl. Crystallogr. **32**, 837 (1999).
[30] G. M. Sheldrick, A short history of SHELX, Acta Crystallogr. Sect. A Found. Crystallogr. **64**, 112 (2008).
[31] See Supplemental Material at http://link.aps.org/supplemental/10.1103/vjv9-twm9 for details of the electron-density analysis, including atomic electron-density maxima, fractional atomic coordinates, net atomic charges, anisotropic displacement parameters, electron-density and deformation-density maps, bond-critical-point properties, atomic basin volumes, the refinement and disorder model of β-KNO_3, and the phenomenological description of the free energy, which includes Ref. [32].
[32] R. M. Lynden-Bell, M. Ferrario, I. R. McDonald, and E. Salje, A molecular dynamics study of orientational disordering in crystalline sodium nitrate, J. Phys. Condens. Matter **1**, 6523 (1989).
[33] A. Volkov, P. Macchi, L. J. Farrugia, C. Gatti, P. R. Mallinson, T. Richter, and T. Koritsanszky, A computer program package for multipole refinement, topological analysis of charge densities and evaluation of intermolecular energies from experimental and theoretical structure factors (2024), https://www.chem.gla.ac.uk/∼louis/xd-home/.
[34] Z. Su and P. Coppens, Nonlinear least-squares fitting of numerical relativistic atomic wave functions by a linear combination of slater-type functions for atoms with $Z = 1$–36, Acta Crystallogr. Sect. A **54**, 646 (1998).
[35] B. Dittrich, P. Munshi, and M. A. Spackman, Invariom-model refinement of L-valinol, Acta Crystallogr. Sect. C **62**, o633 (2006).
[36] M. Woińska and P. M. Dominiak, Transferability of atomic multipoles in amino acids and peptides for various density partitions, J. Phys. Chem. A **117**, 1535 (2013).
[37] Y. V. Nelyubina, A. A. Korlyukov, K. A. Lyssenko, and I. V. Fedyanin, Transferable aspherical atom modeling of electron density in highly symmetric crystals: A case study of alkali-metal nitrates, Inorg. Chem. **56**, 4688 (2017).
[38] S. Mondal, Charge transfer and fractional bonds in stoichiometric boron carbide, Chem. Mater. **29**, 6191 (2017).
[39] V. Petricek, M. Dusek, and L. Palatinus, Crystallographic computing system JANA2006: General features, Z. Kristallogr. **229**, 345 (2014).
[40] L. Palatinus, S. J. Prathapa, and S. van Smaalen, EDMA: A computer program for topological analysis of discrete electron densities, J. Appl. Crystallogr. **45**, 575 (2012).
[41] M. S. Schmøkel, S. Cenedese, J. Overgaard, M. R. V. Jørgensen, Y.-S. Chen, C. Gatti, D. Stalke, and B. B. Iversen, Testing the concept of hypervalency: Charge density analysis of K_2SO_4, Inorg. Chem. **51**, 8607 (2012).
[42] A. Putnis, E. Salje, S. A. T. Redfern, C. A. Fyfe, and H. Strobl, Structural states of Mg-cordierite I: Order parameters from synchrotron X-ray and NMR data, Phys. Chem. Miner. **14**, 446 (1987).
[43] U. Müller, Relating crystal structures by group–subgroup relations, in *International Tables for Crystallography*, edited by H. Wondratschek and U. Müller, Symmetry Relations Between Space Groups, Vol. A1 (John Wiley & Sons, Ltd., Chichester, 2010), pp. 44–56.
[44] O. Akay Sefer and H. Yurtseven, Temperature dependence of the order parameter and dielectric susceptibility for the ferroelectric–incommensurate–paraelectric phase transitions in $NaNO_2$, Low Temp. Phys. **52**, 279 (2026).

[45] M. A. Carpenter, C. J. Howard, B. J. Kennedy, and K. S. Knight, Strain mechanism for order-parameter coupling through successive phase transitions in $PrAlO_3$, Phys. Rev. B **72**, 024118 (2005).
[46] J. W. Harter, Z. Y. Zhao, J.-Q. Yan, D. G. Mandrus, and D. Hsieh, A parity-breaking electronic nematic phase transition in the spin-orbit coupled metal $Cd_2Re_2O_7$, Science **356**, 295 (2017).
[47] M. H. Brooker, Raman study of the structural properties of KNO_3(II), Can. J. Chem. **55**, 1242 (1977).